



μ -near-zero supercoupling

João S. Marcos,¹ Mário G. Silveirinha,^{1,*} and Nader Engheta²

¹*Department of Electrical Engineering, University of Coimbra, Instituto de Telecomunicações, 3030-290, Coimbra, Portugal*

²*Department of Electrical and Systems Engineering, University of Pennsylvania, Philadelphia, Pennsylvania 19104-6314, USA*

(Received 30 July 2014; revised manuscript received 14 April 2015; published 11 May 2015)

Here we theoretically predict and experimentally verify that permeability μ -near-zero (MNZ) materials give the opportunity to supercouple waveguides with highly mismatched cross sections. Rather distinct from the supercoupling provided by permittivity-near-zero materials we discovered several years ago, the MNZ supercoupling can take place when the transition channel cross section is much wider than that of the input and output waveguides. We develop a simple analytical model that captures the physical mechanisms that enable this remarkable effect. The MNZ supercoupling effect is experimentally verified with rectangular waveguide technology by mimicking the μ -near-zero response with the help of cylindrical split ring resonators.

DOI: [10.1103/PhysRevB.91.195112](https://doi.org/10.1103/PhysRevB.91.195112)

PACS number(s): 78.67.Pt, 41.20.Jb, 42.70.Qs

I. INTRODUCTION

Materials with near-zero permittivity (ENZ) and/or near-zero permeability (MNZ) offer the opportunity to have *in-phase* oscillations of the electromagnetic field in a spatial range with dimensions much larger than the characteristic wavelength of light in free space for a certain frequency of oscillation [1–3]. These collective in-phase oscillations of the structural unities of the material (e.g., atoms in case of natural media, and “inclusions” in case of metamaterials) effectively synchronize the responses of “distant” points of the material, and in this way enable remarkable phenomena such as supercoupling through narrow channels and bends [2,4–7], enhanced radiation rates by charged beams, quantum emitters, and other sources [8–10], tailoring the radiation phase pattern [11], trapping light in open cavities with lifetimes not limited by radiation loss [12], and linear dispersing photonic bands [13].

Of particular relevance here is the tunneling effect predicted in Ref. [2], and experimentally validated in Refs. [4–7], wherein electromagnetic waves are squeezed through ENZ filled channels with very low reflectivity, such that in the absence of material loss, the transmission level through the ENZ channel can approach 100% when the transverse cross section of the channel is made narrower and narrower. Differently, the playground of this work consists of a parallel plate waveguide with metallic walls—e.g., modeled as perfect electric conductors (PEC)—with a transition filled with a material with near-zero permeability [$\mu(\omega) \approx 0$] [Fig. 1(a)]. Notably we demonstrate in what follows that the physics of the metallic waveguide with the MNZ transition is quite rich and fundamentally different from that of the waveguide with an ENZ channel. It is important to highlight that this problem cannot be reduced using a duality transformation to the structures of Ref. [2]. Indeed, a duality mapping can transform an ENZ material into a MNZ material, but it simultaneously transforms the PEC walls into perfect magnetic conductors (PMC) [14]. MNZ waveguides that differ by a duality transformation from our earlier works [2] were theoretically and experimentally studied in Ref. [15].

II. THEORY

To begin with, we develop a simple analytical model to characterize the wave reflection and transmission in the considered waveguide. Analogous to Ref. [16], each section of the parallel plate waveguide can be modeled as a transmission line with per unit of length (p.u.l.) capacitance $C = \epsilon w/d$ and p.u.l. inductance $L = \mu d/w$, with ϵ, μ being the parameters of the filling material, d is the distance between the plates, and w is the width of the waveguide along the z direction. Thus, the propagation constant and the characteristic impedance of the i th waveguide section satisfy $\beta_i = \omega\sqrt{L_i C_i}$ and $Z_{c,i} = \sqrt{L_i/C_i}$, such that

$$Z_{c,i} = \eta_i \frac{d_i}{w}, \quad \beta_i = \omega\sqrt{\epsilon_i \mu_i}, \quad (1)$$

where $\eta_i = \sqrt{\mu_i/\epsilon_i}$ is the intrinsic impedance of the i th material. Neglecting the effect of the transition regions, we can easily determine the reflection (R) and the transmission coefficients (T) using the transmission line theory. Assuming a time variation of the type $e^{-i\omega t}$ the result is

$$R = \frac{i(Z_{c,0}^2 - Z_{c,1}^2) \sin(\beta_1 l)}{2Z_{c,0}Z_{c,1} \cos(\beta_1 l) - i(Z_{c,0}^2 + Z_{c,1}^2) \sin(\beta_1 l)}, \quad (2a)$$

$$T = \frac{2Z_{c,0}Z_{c,1}}{2Z_{c,0}Z_{c,1} \cos(\beta_1 l) - i(Z_{c,0}^2 + Z_{c,1}^2) \sin(\beta_1 l)}, \quad (2b)$$

where the subscript “0” is associated with the input and output waveguides, whereas the subscript “1” is associated with the transition channel. Evidently the condition to have 100% transmission corresponds to the matching of characteristic impedances $Z_{c,0} = Z_{c,1}$. Crucially, from Eq. (1) it is seen that the condition $Z_{c,0} = Z_{c,1}$ is *not* the same as the matching of intrinsic impedances, but rather equivalent to $\eta_0 d_0 = \eta_1 d_1$, and thus it depends on the waveguides height mismatch. Assuming that the input and output waveguides are filled with air, the matching condition can be written explicitly in terms of the material parameters as

$$\frac{\mu_{r1}}{\epsilon_{r1}} = \left(\frac{d_0}{d_1}\right)^2, \quad (3)$$

where μ_{r1}, ϵ_{r1} are the relative permeability and permittivity of the transition channel. In particular, one sees that in the

*To whom correspondence should be addressed: mario.silveirinha@co.it.pt

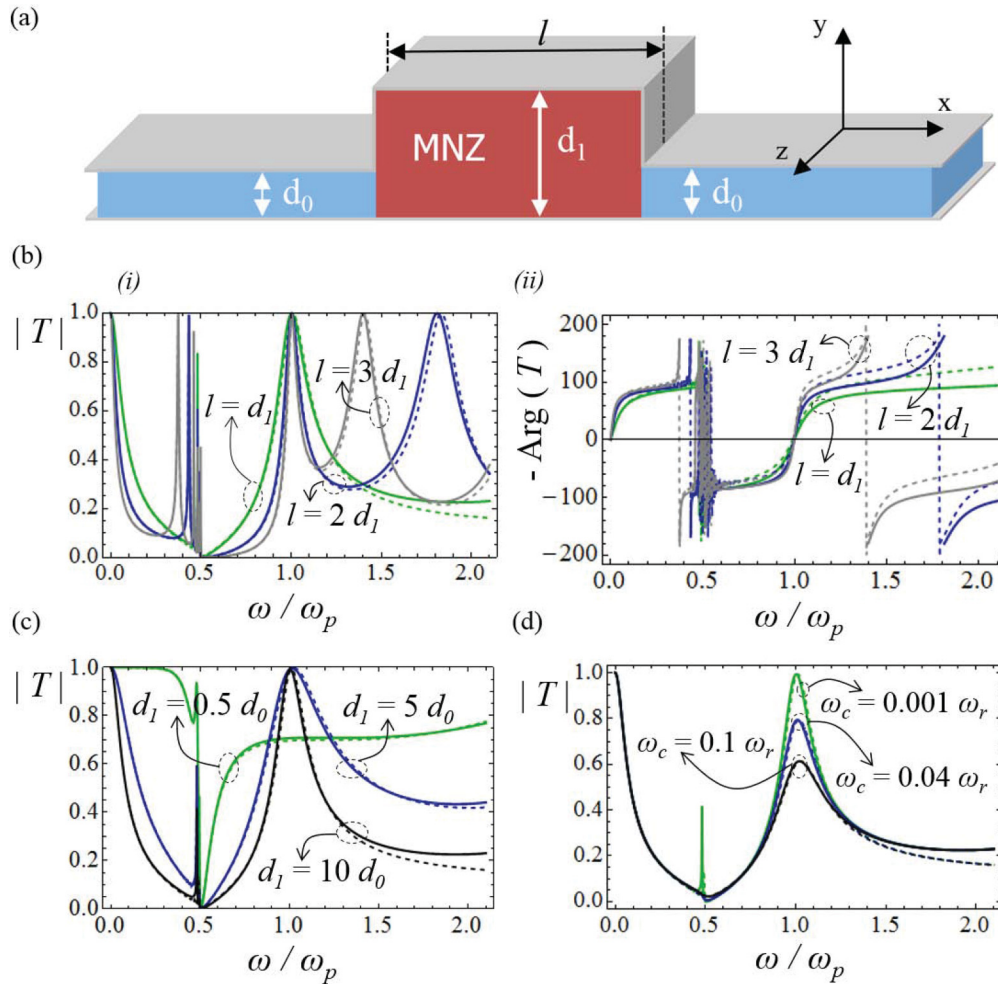


FIG. 1. (Color online) (a) A parallel-plate metallic waveguide has a transition channel filled with a μ -near-zero (MNZ) material. The central section has a height d_1 , and the input and output regions have height d_0 . (b) Transmission coefficient—(i) amplitude and (ii) phase—as a function of frequency for different values of l/d_0 and for $d_1/d_0 = 10$ and $\omega_c/\omega_r = 0.001$. (c) Similar to (b) but for different values of d_1/d_0 and $l/d_0 = 10$ and $\omega_c/\omega_r = 0.001$. (d) Similar to (b) but for different damping frequencies ω_c/ω_r , and $d_1/d_0 = 10$ and $l/d_0 = 10$. Solid lines: Analytical model. Dashed lines: Full wave simulations with CST Microwave Studio® [17].

limit $d_1/d_0 \rightarrow 0$ (i.e., for an extremely narrow channel) the matching condition requires that $\epsilon_{r1} \rightarrow 0$. This is the regime investigated in Ref. [2]. Surprisingly, Eq. (3) reveals another nontrivial possibility of having a supercoupling based on media with zero refractive index. Indeed, in the limit $d_0/d_1 \rightarrow 0$, i.e., for an extremely wide transition channel, it is possible to have a perfect tunneling in the MNZ limit, i.e., for $\mu_{r1} \rightarrow 0$. Note that when $\mu_{r1} = 0$ the transition channel does not support photonic states, and thus it is highly nontrivial to transmit light through a long MNZ channel (hence the designation “supercoupling”).

To unveil the physics underlying the MNZ supercoupling, we take the limit $\mu_{r1} \rightarrow 0$ of Eqs. (2) to find that

$$T = \frac{1}{1 - i \frac{\epsilon_{r1}}{2} \frac{\omega l}{c} \frac{d_0}{d_1}}, \quad R = T - 1. \quad (4)$$

This formula confirms that in the μ -near-zero lossless limit the input and output waveguides may be supercoupled with nearly 100% efficiency, provided the waveguide heights are strongly mismatched and the waveguide is enlarged in the MNZ channel ($d_0/d_1 \rightarrow 0$). For completeness we note that in

the ENZ limit the same analysis gives $T = 1/(1 - i \frac{\mu_{r1}}{2} \frac{\omega l}{c} \frac{d_1}{d_0})$, and thus the ENZ supercoupling requires $d_1/d_0 \rightarrow 0$ (narrow channel) as found in Ref. [2]. It is relevant to mention that in contrast with the $\epsilon \rightarrow 0$ limit, the current problem does not have an exact analytical solution in the $\mu \rightarrow 0$ limit. Indeed, in the $\mu \rightarrow 0$ limit the magnetic field inside the channel is not required to be *exactly* constant in the transition channel as in [2].

To validate our theoretical analysis, we used commercial electromagnetic software [17] that numerically solves the Maxwell’s equations using a finite-integration time-domain numerical technique. In our simulations it was assumed that the permeability of the MNZ channel has a Drude-Lorentz dispersion model such that $\mu_r = 1 + \omega_m^2/(\omega_r^2 - \omega^2 - 2i\omega\omega_c)$, where ω_r and ω_c are the resonant and damping frequencies, and $\omega_m^2 = \omega_p^2 - \omega_r^2$, where ω_p is the frequency wherein the permeability of the material is near zero ($\mu(\omega_p) \approx 0$). Figures 1(b)–1(d) show the computed transmission coefficient for different values of the channel length, channel height, and damping frequency, with $\epsilon_{r1} = 1$, $\omega_r d_0/c = 0.1$, and

$\omega_r = \omega_p/2$. The value ω_p can be arbitrarily fixed and can be regarded as a normalizing constant. As seen, the full wave simulations (dashed lines) agree well with our analytical model (solid lines). The small discrepancies between the two sets of curves for high frequencies are due to the effect of higher-order modes. Particularly, the numerical results confirm that as $d_0/d_1 \rightarrow 0$ [Fig. 1(c)], i.e., as the MNZ channel gets wider and wider, the transmission level at the μ -near-zero frequency $\omega = \omega_p$ is consistently increased. Interestingly, there may be other transmission peaks away from the MNZ regime [see Fig. 1(b) for $\omega/\omega_p > 1.3$] due to Fabry-Perot type resonances. Notably, these transmission peaks are highly sensitive to the specific geometry of the channel, e.g., to the length of the channel [Fig. 1(b)]. Quite differently, in presence of the MNZ material the transmission level is near 100% at $\omega = \omega_p$, independent of the geometry of the channel, provided the height of the MNZ channel is much larger than the height of the input and output waveguides.

Time snapshots of the magnetic and electric fields and of the time averaged Poynting vector calculated at $\omega = \omega_p$ are shown in Fig. 2 for the scenario wherein $d_0/d_1 = 0.1$ and $l = 10d_0$. These plots reveal that the magnetic field in the waveguide is nearly uniform, whereas the electric field is

greatly depressed inside the MNZ region, i.e., $\mathbf{E} \approx 0$. Within our transmission line model, in the $\mu_{r1} \rightarrow 0$ limit the fields in the MNZ waveguide section ($0 < x < l$) satisfy

$$H_z(x) \approx \left[(1 - R) + i \frac{\omega x}{c} \varepsilon_{r1} (1 + R) \frac{d_0}{d_1} \right] \frac{E_y^{\text{inc}}}{\eta_0}, \quad (5a)$$

$$E_y(x) \approx \frac{d_0}{d_1} (1 + R) E_y^{\text{inc}}, \quad (5b)$$

where E_y^{inc} is the amplitude of the incoming wave at the $x = 0$ interface. Thus, when $d_0/d_1 \rightarrow 0$, it follows that $R \rightarrow 0$ and therefore the fields satisfy $H_z \approx E_y^{\text{inc}}/\eta_0$ and $E_y \ll E_y^{\text{inc}}$, in complete agreement with the full wave simulations. Notably, from Eq. (5b) it follows that the electric field in the MNZ channel is a nonzero constant independent of x , and hence the electric field oscillations are synchronized in all points of the transition region, independent of its length l . Moreover, for a lossless structure (ε_{r1} is real valued) the time averaged Poynting vector in the MNZ region satisfies $S_{\text{av},x} = (1 - |R|^2) \frac{d_0}{d_1} S_{\text{av},x}^{\text{inc}}$, with $S_{\text{av},x}^{\text{inc}} = |E_y^{\text{inc}}|^2 / (2\eta_0)$, as required by the conservation of energy. An interesting observation is that for wide channels ($d_0/d_1 \rightarrow 0$) the effect of dielectric loss in the MNZ material may be almost irrelevant, and the transmissivity of the channel may be weakly affected by $\text{Im}\{\varepsilon_{r1}\}$. Indeed, noting that Eqs. (4) and (5) also apply to ε_{r1} complex valued, it is seen that in the limit $d_0/d_1 \rightarrow 0$ and $\mu_{r1} \rightarrow 0$ the dielectric loss is

$$P_{l,e} = \frac{\omega}{2} \text{Im}\{\varepsilon_1\} \int_{\text{channel}} |\mathbf{E}|^2 dV \approx \frac{\omega}{2} \text{Im}\{\varepsilon_1\} l \times w \times d_0 |(1 + R) E_y^{\text{inc}}|^2 \frac{d_0}{d_1}. \quad (6)$$

Thus, the dielectric loss scales with the height of the channel as d_0/d_1 . Clearly the absorption in the MNZ channel is mainly determined by magnetic loss due to $\text{Im}\{\mu_1\} > 0$.

Significantly, for $\mu_1 = 0$ the MNZ material does not support radiative photonic states (with nonzero group velocities), and hence the MNZ supercoupling occurs due to near-field coupling and photon tunneling. Moreover, the field distribution in the MNZ channel is like the field distributions associated with (magnetic) volume plasmons. Volume plasmons are nonradiative natural oscillations of a plasma that occur when $\mu(\omega) = 0$, i.e., at $\omega = \omega_p$. They are characterized by $\mathbf{H} \neq 0$ and $\mathbf{E} = 0$, similar to field distribution in Eq. (5) where the magnetic field is dominant in the limit $d_0/d_1 \rightarrow 0$.

III. EXPERIMENTAL VERIFICATION

In order to experimentally verify the MNZ supercoupling, we emulated the two-dimensional propagation scenario of Fig. 1 with microwave waveguide technology (Fig. 3). Each prototype consists of three interconnected hollow (air-filled) metallic waveguides with a height mismatch such that $d_0/d_1 = 1/10$ and $d_0 = 3.7$ mm. The width of the waveguides is $w = 90$ mm. The incident wave is the dominant TE_{10} mode with the cut-off frequency $f_{10} = 1.67$ GHz, and is radiated by a short monopole inserted into the waveguide (P1 in Fig. 3). The ‘‘main body’’ of the waveguides was milled in an aluminum block with

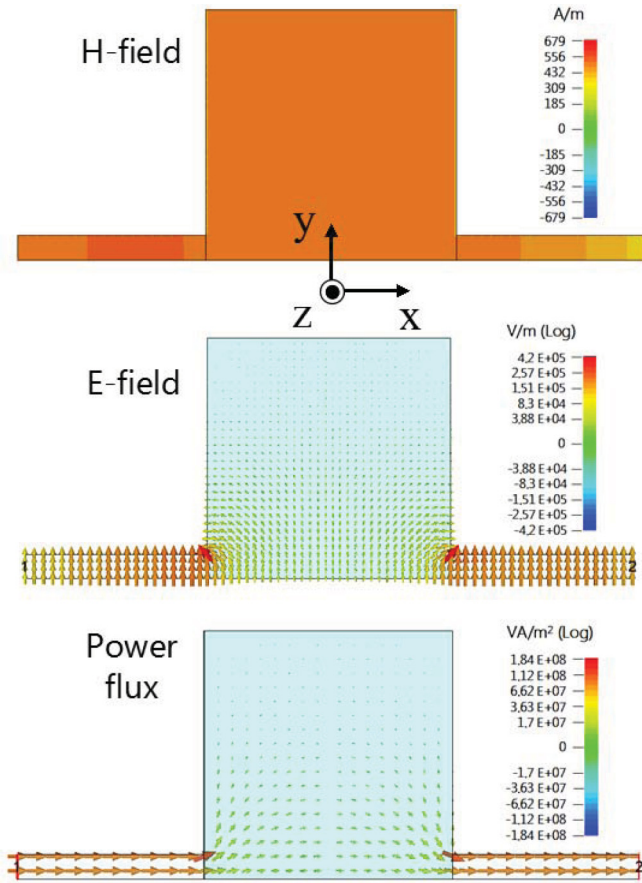


FIG. 2. (Color online) Top panel: Time snapshot of the z component of the magnetic field. Middle panel: Time snapshot of the in-plane electric field. Bottom panel: Time averaged Poynting vector. It is assumed that $d_1/d_0 = 10$, $l/d_0 = 10$, $\omega_c/\omega_r = 0.001$, and the oscillation angular frequency is $\omega = \omega_p$.

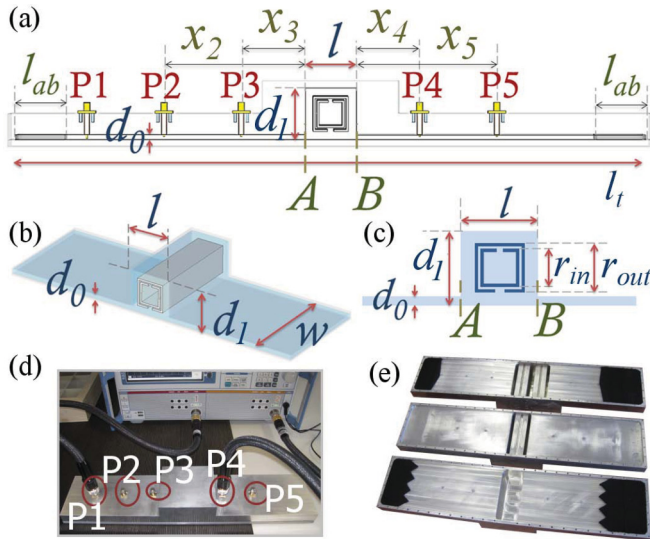


FIG. 3. (Color online) (a) Side view of the waveguide prototype with a single SRR in the MNZ channel with $l = 37$ mm. The structure has a total length $l_t = 447$ mm and is excited by a small monopole (P1) corresponding to the inner conductor of a rear mount type SMA jack. The short monopoles P2–P5 are used to probe the fields in the waveguide and to compute the S parameters referred to the A and B planes. The distance between the probes and the A and B planes are $x_2 = x_5 = 100$ mm and $x_3 = x_4 = 45$ mm. Microwave absorbers with length $l_{ab} = 35$ mm are placed at the waveguide end walls. (b) Perspective view of the structure. The lateral width is $w = 90$ mm and the heights are $d_1 = 37$ mm and $d_0 = 3.7$ mm. (c) Detail of the geometry of the split-ring resonator. The square side length for the inner and outer rings is $r_{in} = 19.5$ mm and $r_{out} = 25$ mm, respectively. The ring thickness is 1.5 mm, the separation between rings is 1.5 mm, and the split width is 1/5 of the square side length. (d) Photo of the experimental setup showing the vector network analyzer and one of the prototypes in case of a transmission measurement from P1 to P4. (e) Overview of the three prototypes with the bottom walls removed. Top: Prototype with two cylindrical SRRs. Middle: Prototype with a single cylindrical SRR. Bottom: Prototype with the empty channel. The pyramidal shaped microwave absorbers can be seen at the waveguide end walls.

electrical conductivity $\sigma \sim 3.5 \times 10^7$ S/m. The bottom wall is attached to the main body with several screws to ensure a good contact between the parts and reduce the possibility of having air gaps (Fig. 3). Small monopole antenna probes (P2–P5) are inserted into the waveguide top wall to characterize the S parameters. Microwave absorbers (*Eccosorb LS-26*) were placed at the waveguide ends to minimize reflections from the end walls. The S parameters, referring to the ports of the short monopole probes (P1–P5), were measured with a vector network analyzer (R&S ZBV-20). The post processing of this data [specifically of the transmission coefficients from the feeding monopole (P1) to the four sensing probes (P2–P5)] enables calculating the S_{11} and S_{21} parameters referred to the transition channel input and output planes (A and B planes in Fig. 3). The reader can find more details about the de-embedding method in Ref. [5].

In our design, the μ -near-zero response of the transition channel is mimicked with the help of cylindrical split-ring

resonators (SRRs) with a square cross section (Fig. 3). The inner and outer rings of the cylindrical SRRs are made of commercially available aluminum tubes. A longitudinal strip was cut from the tubes to create the desired splits. The rings are soldered to the main body of the structure (Fig. 3). It is known that these resonant inclusions provide a strong magnetic response when the perimeter of the ring cross section approaches $\lambda/2$ [18]. Thus, we can estimate that the ring will have a strong magnetic response when $\beta_{10}p = \pi$ where $p \sim 4 \times 25$ mm is the perimeter of the outer ring and β_{10} is the propagation constant of the TE_{10} mode. This rough estimation predicts that a strong magnetic response should occur at $f_p \sim 1.3 f_{10}$. We used a quite minimalist implementation of the MNZ material such that in the first prototype the MNZ channel is filled with a single SRR, and in the second prototype the MNZ channel contains two SRRs (Fig. 3). The main reason is that it is difficult to accommodate many inclusions in the transition channel given its subwavelength dimensions. Nevertheless, because in the MNZ regime the fields in the transition channel are expected to be nearly constant, it is not too critical to have a large number of inclusions in the channel to reproduce the physical mechanisms that dictate the MNZ supercoupling. The transition channel in the prototype with a single SRR has the length $l = d_1 = 37$ mm, and in the prototype with two SRRs has the length $l = 2d_1 = 74$ mm. We also fabricated a third prototype such that the transition channel is empty and has $l = d_1$.

Figure 4(a) depicts the measured S_{21} coefficient (amplitude and phase) as a function of the normalized frequency. The solid lines represent the experimental results and the dashed lines the simulation results obtained with CST Microwave Studio® [17]. In the CST simulations the waveguide walls are modeled using an impedance boundary condition, consistent with the surface impedance of aluminum. The excitation is based on two CST waveguide ports placed at the ends of the input and output waveguides. One of the waveguide ports generates the TE_{10} fundamental mode used to excite the structure. The waveguide ports absorb the waves reflected by and transmitted through the channel and allow extracting the relevant scattering parameters. There is an overall good agreement between the simulations and the measurements, with the deviations being attributed to fabrication tolerances and to an imperfect contact between the main body of the structure and the bottom wall. As seen in Fig. 4(a), for the prototype with a single SRR inclusion (green lines) there is a transmission peak around $f = 1.1 f_{10}$ (which is reasonably consistent with the rough estimation $1.3 f_{10}$ previously discussed). Importantly, at the same frequency where the transmission peaks, the phase of the S_{21} parameter vanishes, indicating an infinite phase velocity across the transmission channel and revealing in this manner the characteristic fingerprint of the MNZ supercoupling regime. Without the SRR inclusion [blue lines in Fig. 4(a)] the transmission level drops sharply due to the strong height mismatch between the waveguide sections. To demonstrate that the MNZ channel keeps its zero phase delay and tunneling characteristics independent of its length, we show in Fig. 4(b) the S_{21} parameter for the prototype with two SRR inclusions (black lines). Consistent with the results of Fig. 1, it is seen that doubling the length of the channel results in a tiny shift in the frequency wherein the supercoupling

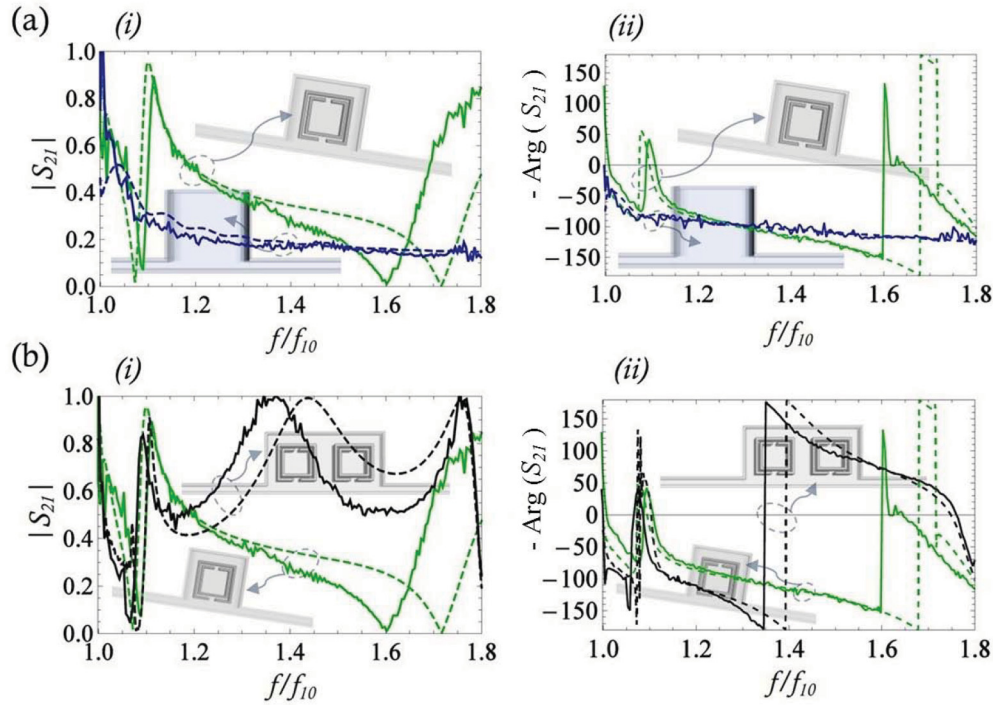


FIG. 4. (Color online) Amplitude (i) and phase (ii) of the transmission coefficient (S_{21}) as a function of frequency. Solid lines: Experimental results. Dashed lines: Numerical simulations with CST Microwave Studio[®]. (a) Results for the prototype with a single SRR (green lines) superimposed on the results for the empty waveguide prototype (blue lines). (b) Results for the prototype with two SRRs (black lines) superimposed on the results for the prototype with a single SRR (green lines). Note that the green lines are repeated in (b) to ease the comparison between the different setups.

takes place. To confirm the magnetic origin of the MNZ supercoupling, we represent in Fig. 5 the density plots of the magnetic field in the structure with two SRRs calculated at the frequency wherein there is zero-phase delay. As seen, the magnetic field distribution is consistent with that associated with the magnetic resonance of the SRRs, while the zero-phase delay ensures that the effective permeability is indeed near

zero. Moreover, the magnetic field distributions are rather similar in the vicinity of the two SRRs in the MNZ regime [Fig. 5(b)]. This property is the microscopic counterpart of having a constant macroscopic magnetic field in the channel (Fig. 2). It is noted that the supercoupling effect reported here is not based on a resonance of the permeability response (which, in the framework of the Lorentz model considered previously, occurs at the frequency ω_r with $\mu \rightarrow \infty$), but rather on the MNZ response (which occurs at ω_p). In our metamaterial realization ω_r and ω_p are closely spaced but they can be distinguished unambiguously: ω_p may be identified with the frequency wherein the phase of the S_{21} parameter crosses zero, whereas ω_r is the frequency slightly below ω_p wherein the phase slope is very large.

To further support that our metamaterial waveguide does indeed mimic the response of an MNZ channel, we did a few numerical control experiments using CST Microwave Studio [17]. In the first numerical experiment we considered a setup analogous to that reported in Fig. 4(a), but such that the gaps of the SRR are closed. This structural modification effectively eliminates the magnetic response of the SRR. The calculated transmission coefficient for this scenario is reported in Fig. 6(a). As seen, when the magnetic response is suppressed the transmission peak with zero-phase delay around $f = 1.1f_{10}$ also disappears, demonstrating that the supercoupling effect is rooted in the magnetic response of the waveguide inclusions. In the second control numerical experiment we studied the influence of centering the transition channel about the axis of the input and output waveguides. This test serves to exclude the possibility that the bottom

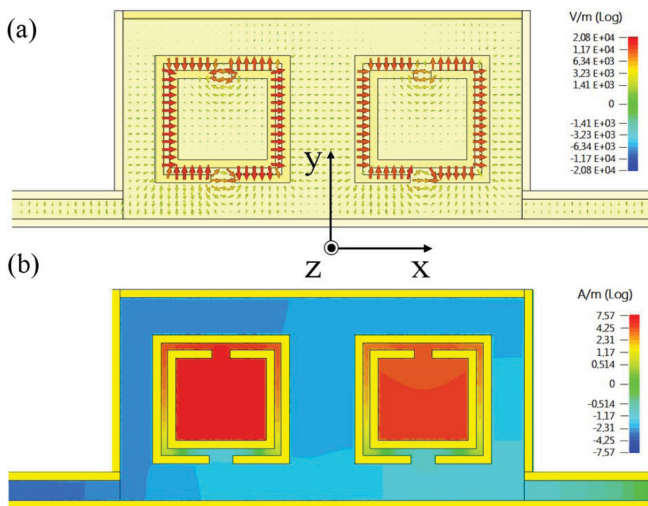


FIG. 5. (Color online) Time snapshots of the simulated electromagnetic fields at the midplane of the waveguide with two SRRs. The oscillation frequency coincides with the MNZ supercoupling regime. (a) In-plane electric field. (b) z component of the magnetic field.

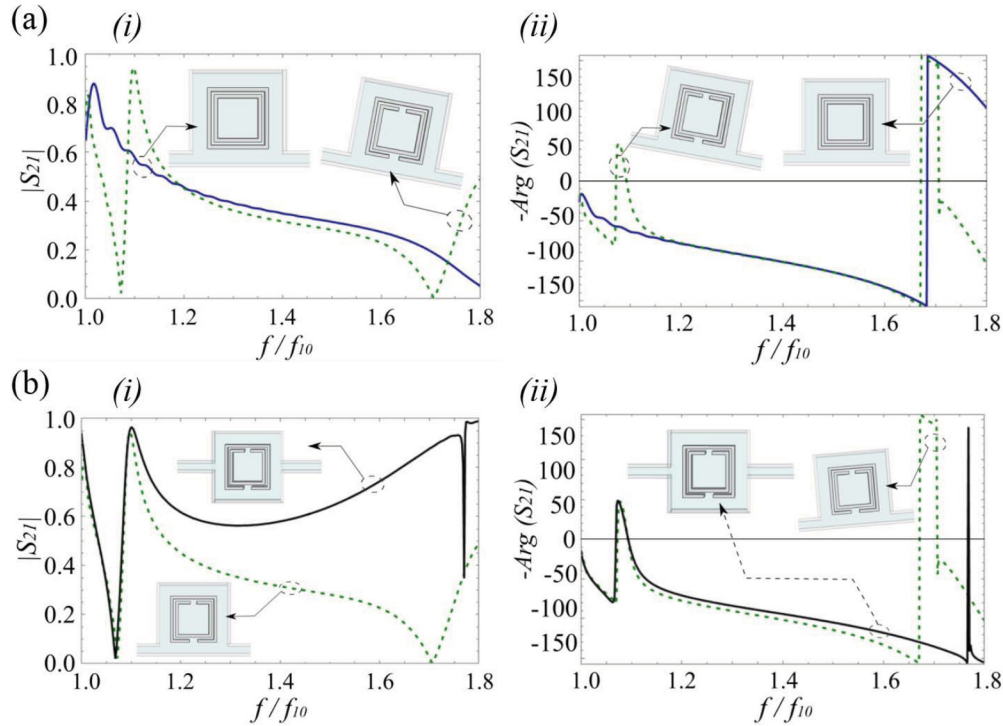


FIG. 6. (Color online) Amplitude (i) and phase (ii) of the transmission coefficient (S_{21}) as a function of the frequency. (a) Effect of closing the SRR gap. (b) Effect of centering the input and output waveguides. The dashed (green) curves are the same as in Fig. 4.

arms of the SRR could channel the TE_{10} mode across the transition. The results of Fig. 6(b) reveal that centering the transition channel has no relevant influence on the transmission level for $f < 1.1 f_{10}$. In particular, the supercoupling effect with zero-phase delay around $f \approx 1.1 f_{10}$ is unaffected by the coupling position. For frequencies larger than $1.1 f_{10}$ (away from the MNZ regime) the coupling through the central section tends to enhance the transmission level. We also verified (not shown here) that rotating the SRR by 90° around its symmetry axis has no sensible influence on the supercoupling effect around $1.1 f_{10}$.

IV. CONCLUSION

In conclusion, using a transmission line model it was theoretically demonstrated that MNZ materials provide virtually perfect matching between waveguides with highly mismatched cross sections. It was shown in the MNZ supercoupling regime the electromagnetic field is dominantly magnetic, and is like the field distributions associated with volume (magnetic) plasmons. The MNZ supercoupling was experimentally verified in a rectangular waveguide configuration wherein the μ -near-zero response is mimicked by cylindrical

split-ring resonator inclusions. Due to the zero-phase delay in the channel, this new supercoupling regime, when designed for the proper wavelength, may enhance the emission by a collection of magnetic light sources (e.g., magnetic dipole emitters) placed within the MNZ channel. Indeed, due to the long wavelength in the channel the different emitters may be excited in phase and thus the radiated fields will add up. At the same time, the emission to electric dipole modes is expected to be depressed because the electric field may be rather weak in the MNZ cavity. Hence, an MNZ material may enable boosting the usually quite weak emission by magnetic-dipole transitions in atoms and molecules as compared to the emission by electric-dipole transitions, and this may have applications in sensing and spectroscopy [19,20].

ACKNOWLEDGMENTS

This work is supported in part by Fundação para a Ciência e a Tecnologia Grant No. PTDC/EEI-TEL/2764/2012. N.E. acknowledges the partial support from the U.S. Office of Naval Research (ONR) Office of Naval Research (ONR) Multidisciplinary University Research Initiatives (MURI) Grant No. N00014-10-1-0942.

[1] R. W. Ziolkowski, *Phys. Rev. E* **70**, 046608 (2004).
 [2] M. G. Silveirinha and N. Engheta, *Phys. Rev. Lett.* **97**, 157403 (2006); *Phys. Rev. B* **75**, 075119 (2007); *Phys. Rev. Lett.* **102**, 103902 (2009).
 [3] N. Engheta, *Science* **340**, 286 (2013).

[4] B. Edwards, A. Alù, M. E. Young, M. Silveirinha, and N. Engheta, *Phys. Rev. Lett.* **100**, 033903 (2008).
 [5] B. Edwards, A. Alù, M. G. Silveirinha, and N. Engheta, *J. Appl. Phys.* **105**, 044905 (2009).

- [6] Q. Cheng, R. Liu, D. Huang, T. J. Cui, and D. R. Smith, *Appl. Phys. Lett.* **91**, 234105 (2007).
- [7] R. Liu, Q. Cheng, T. Hand, J. J. Mock, T. J. Cui, S. A. Cummer, and D. R. Smith, *Phys. Rev. Lett.* **100**, 023903 (2008).
- [8] A. Alù and N. Engheta, *Phys. Rev. Lett.* **103**, 043902 (2009).
- [9] E. J. R. Vespeur, T. Coenen, H. Caglayan, N. Engheta, and A. Polman, *Phys. Rev. Lett.* **110**, 013902 (2013).
- [10] A. M. Mahmoud and N. Engheta, *Nat. Commun.* **5**, 5638 (2014).
- [11] A. Alù, M. G. Silveirinha, A. Salandrino, and N. Engheta, *Phys. Rev. B* **75**, 155410 (2007).
- [12] M. G. Silveirinha, *Phys. Rev. A* **89**, 023813 (2014).
- [13] X. Huang, Y. Lai, Z. H. Hang, H. Zheng, and C. T. Chan, *Nat. Mater.* **10**, 582 (2011).
- [14] J. D. Jackson, *Classical Electrodynamics*, 3rd ed (John Wiley and Sons, New York, 2001).
- [15] H. F. Ma, J. H. Shi, Q. Cheng, and T. J. Cui, *Appl. Phys. Lett.* **103**, 021908 (2013).
- [16] A. Alù, M. G. Silveirinha, and N. Engheta, *Phys. Rev. E* **78**, 016604 (2008).
- [17] CST Microwave Studio™ 2014, <http://www.cst.com>
- [18] J. B. Pendry, A. J. Holden, D. J. Robbins, and W. J. Stewart, *IEEE Trans. Microwave Theory Tech.* **47**, 2075 (1999).
- [19] S. Karaveli and R. Zia, *Opt. Lett.* **35**, 3318 (2010).
- [20] T. H. Taminiau, S. Karaveli, N. F. van Hulst, and R. Zia, *Nat. Commun.* **3**, 979 (2012).